

Simulation of colloidal fouling by coupling a dynamically updating velocity profile and electric field interactions with Force Bias Monte Carlo methods for membrane filtration

Paul M. Boyle^a, Brent C. Houchens^{a,*}, Albert S. Kim^{b,c}

^a Department of Mechanical Engineering & Materials Science, Rice University, 6100 Main Street, MS-321, Houston, TX 77005, United States

^b Department of Civil and Environmental Engineering, University of Hawaii at Manoa, 2540 Dole Street, Holmes 383, Honolulu, HI 96822, United States

^c Department of Chemical Engineering, Kyung Hee University, Gyeonggi-do 449-701, South Korea

ARTICLE INFO

Article history:

Received 8 December 2011

Accepted 27 October 2012

Available online xxxxx

Keywords:

Membrane fouling

Crossflow filtration

Force Bias Monte Carlo

Generalized Newtonian fluid

ABSTRACT

Pressure-driven flow through a channel with membrane walls is modeled for high particulate volume fractions of 10%. Particle transport is influenced by Brownian diffusion, shear-induced diffusion, and convection due to the axial crossflow. The particles are also subject to electrostatic double layer repulsion and van der Waals attraction, from both particle–particle and particle-membrane interactions. Force Bias Monte Carlo (FBMC) simulations predict the deposition of the particles onto the membranes, where both hydrodynamics and the change in particle potentials determine the probability that a proposed move is accepted. The particle volume fraction is used to determine an apparent local viscosity observed by the continuum flow. As particles migrate, the crossflow velocity field evolves in quasi-steady fashion with each time instance appearing fully developed in the downstream direction. Particles subject to combined hydrodynamic and electric effects (electrostatic double layer repulsion and van der Waals attraction) reach a more stable steady-state as compared to systems with only hydrodynamic effects considered. As expected, at higher crossflow Reynolds numbers more particles remain in the crossflow free stream.

© 2012 Published by Elsevier Inc.

1. Introduction

Water quality and availability are pressing issues with over 1 billion people worldwide lacking access to safe, reliable drinking water. As many as five million die each year of waterborne diseases due to unclean water sources and poor sanitation and hygiene [1]. A range of filtration methods including reverse osmosis (RO), microfiltration and nanofiltration, offer promise in providing potable water. In addition to debris and large contaminants, some membrane filtration can remove biological contaminants such as viruses and bacteria. RO membranes can even be used to remove salts, generating potable water from saline or brackish water. However, all filtration techniques are all susceptible to fouling. Once fouling begins, the systems must be operated at higher pressure to maintain a constant permeate flux, requiring increased power consumption.

Before full-scale, multi-contaminant systems can be fully understood, it is necessary to investigate the physics of single species fouling in simple geometries. The motivation of this study is to demonstrate coupling of a continuum crossflow to a discrete

Monte Carlo simulation and evaluate the validity of such a method for a relatively high (10%) volume fraction of foulant, such as might be present before any pretreatment. Future simulations will predict fouling observed in small-scale laboratory systems such as those of Contreras et al. [2a,b] Faibish et al. [3] and Wang and Tara-bara [4]. The geometry of the flow cell, membrane characteristics and foulants described here mimic the geometry of these experiments, but with a high volume fraction of particulates to better demonstrate the impact on the flow and particle migration. Here results are presented for symmetric cells with membranes on both the top and bottom boundaries. In future simulations, fouling of just one surface will be investigated to better compare to experiments.

Force Bias Monte Carlo (FBMC) methods are used to model particle movement. The hydrodynamics that govern particle motion are well documented [5–7], and several components contribute to the total effect. These include Brownian and shear-induced diffusion, as well as hydrodynamic drag forces. Leighton and Acrivos [7] noted that shear-induced diffusion “arises from the random motion of the particles across streamlines due to the inter-particle interactions which occur as a suspension is sheared”. These diffusive effects have been considered in previous work [6] and are refined here to provide more accurate predictions. Additionally, the

* Corresponding author.

E-mail address: houchens@rice.edu (B.C. Houchens).

velocity profile is updated after each Monte Carlo (MC) step, accounting for the impact of local particle concentration on apparent viscosity.

In addition to the hydrodynamic forces, particle–particle and particle-membrane electric interactions are also considered and influence the migration of the particles in the flow cell. The two interactions examined include van der Waals and electrostatic double layer potentials. The electrostatic potentials are repulsive between objects of the same sign charge (as assumed here). Van der Waals potentials are attractive forces, drawing particles together and toward the membranes and partially offsetting the electrostatic repulsion. In general, the two interactions do not necessarily cancel. It will be shown that these electric interactions damp the randomness in the MC steps.

Here extreme parameters are investigated to describe the impact due to very high contaminant concentrations (10% volume fraction of particles). First cases with just electrostatic and van der Waals forces are considered, without flow. Then a case with no electrostatic or van der Waals interactions is considered to investigate purely hydrodynamic effects. Finally, electrostatic, van der Waals and hydrodynamics are considered. With these limiting cases as benchmarks, future studies will treat more realistic volume fractions for membrane filtration after pretreatment and will attempt to parameterize the impact over a range of charges (for particles and membranes), membrane surface roughness, and particle size distributions.

2. Problem statement, interactions and assumptions

The channel geometry used in the simulations is shown in Fig. 1. The mesh areas (top and bottom) indicate the membrane surfaces of the flow channel, through which there is small perme-

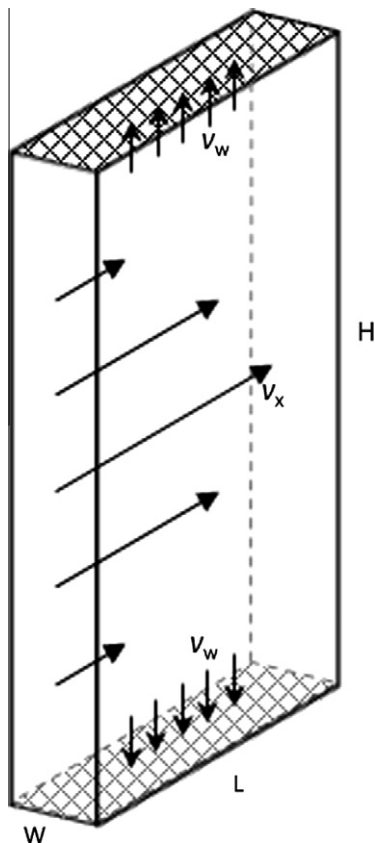


Fig. 1. Channel geometry in dimensional coordinates.

ate outflow. These act as reflective boundaries for particles, which are assumed to be perfectly rejected. The particle centers can only approach to within a radius to the membrane. Periodic conditions are applied on the remaining boundaries. Particles in the flow are subject to many-body hydrodynamic, electrostatic and van der Waals forces, as well as force bias due to the flow.

2.1. Hydrodynamic forces

Particles in the flow are subject to hydrodynamic forces. The velocity normal to the membrane v_z is given by Berman [8] as:

$$v_z(z) = v_w \left[\frac{z}{2}(3 - z^2) - \frac{Re_{\perp}}{280} z(2 - 3z^2 + z^6) \right] \quad (1)$$

where Re_{\perp} is the Reynolds number based on v_z , v_w is the permeate velocity (here taken to be constant), and z is the normalized channel height, scaled such that it is 0 at the center of the channel and +1 and -1 at the top and bottom membrane surfaces, respectively. Assuming that Re_{\perp} of the permeate flow is sufficiently small, as in previous work [6], the permeate profile which convects particles to the membrane surfaces simplifies to $v_z(z) \simeq v_w(3z - z^3)/2$. This profile also assumes incompressible, laminar, steady state flow, in which the presence of particles on the membrane are neglected. This velocity profile is used in conjunction with Happel's sphere-in-cell model and Brownian and shear-induced diffusivities to generate the hydrodynamic force in z that drags particles toward or pushes particles away from the membranes [5]. The crossflow velocity is treated as an unknown and is solved using the one-dimensional momentum equation as discussed in Section 3.1. The hydrodynamic force normal to the membranes is:

$$\mathbf{F}_h = \frac{k_b T v_z(z) K^{-1}(\phi)}{D_B + D_{SI}} \hat{\mathbf{z}} \quad (2)$$

where D_B is the Brownian diffusivity, D_{SI} is the shear-induced diffusivity in the normal direction, K is the sedimentation coefficient that depends on the volume fraction ϕ of the spherical particles in suspension, and K^{-1} is approximated by Happel's model as:

$$K^{-1}(\phi) = \frac{6 + 4\phi^{5/3}}{6 - 9\phi^{1/3} + 9\phi^{5/3} - 6\phi^2} \quad (3)$$

which varies as shown in Fig. 2a. The hydrodynamic force in the crossflow (x) direction is accounted for by the envelope of possible random moves in the Force Bias Monte Carlo method, discussed in Section 3.3.

The Brownian diffusivity is given as:

$$D_B = \frac{k_b T}{6\pi\mu R} S(\phi) \quad (4)$$

where $S(\phi) = \partial(\phi Z(\phi))/\partial\phi$ and Z represents the osmotic compressibility, which in hard-sphere systems is given by the Carnahan–Starling equation [9]:

$$Z(\phi) = \frac{1 + \phi + \phi^2 - \phi^3}{(1 - \phi)^3} \quad (5)$$

Because of the relatively low volume fraction of particles, S is assumed constant with a value of unity [9]. The shear-induced diffusivity can be expressed as:

$$D_{SI} = \dot{\gamma}(z) R^2 \hat{D}(\phi), \quad (6)$$

where $\dot{\gamma}$ is the shear rate in the channel, and \hat{D} is the dimensionless shear-induced correction factor experimentally found to be:

$$\hat{D}(\phi) = \frac{1}{3} \phi^2 \left(1 + \frac{1}{2} e^{8.8\phi} \right) \quad (7)$$

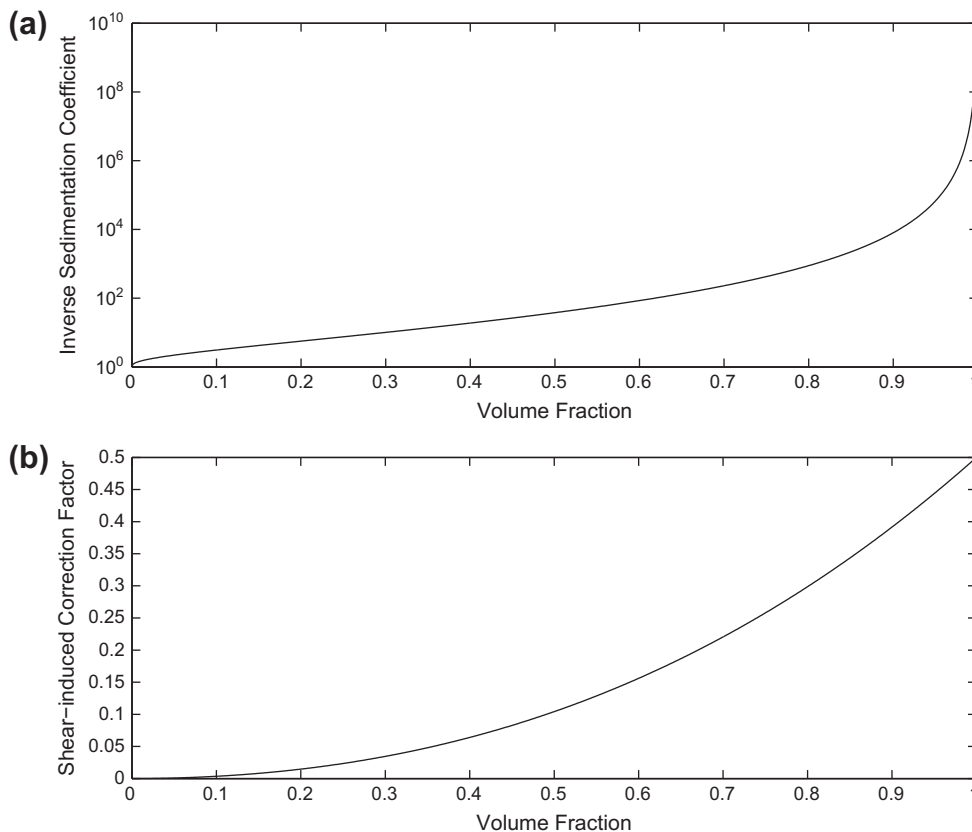


Fig. 2. (a) Inverse sedimentation coefficient $K^{-1}(\phi)$ (Happel correction factor); (b) Shear-induced correction factor, $\hat{D}(\phi)$, versus volume fraction ϕ .

as in [7,10–11]. It should be noted that Eqs. (4) and (6) are for use in systems where the only interactions are between hard-spheres. These are, however, used in this work as an approximation when weak electric interactions are present. The shear-induced correction factor $\hat{D}(\phi)$ varies with ϕ as shown in Fig. 2b. The densities of the particles are taken to be that of BSA (Bovine Serum Albumin), with density 1372 kg/m^3 corresponding to a volume to mass ratio of 0.729 mL/g [12]. Though the particle density does not match that of water, gravitational effects were neglected, as supported by experiments. For example, in the membrane cell experiments of Li et al. using BSA [2], the membrane is at the top of the cell, thus gravity should mitigate fouling if it is non-negligible. In fact, fouling is still observed due to hydrodynamic transport of particulates to the membrane surface. The only significant force normal to the membrane (acting over significant distance) is hydrodynamic, as described by Eq. (2).

2.2. Van der Waals interactions and electrostatic forces

The particles are also subject to van der Waals attraction and electrostatic double layer repulsion. All simulation results presented here are for particles and membranes with the same charge to investigate the maximum electrostatic repulsion. To explain the dynamic simulation of particles in the channel a detailed description of the potential functions between two particles, and between a particle and the membrane surface, are included below. In all simulations in this paper, nondimensionalized potential equations are used by taking advantage of the mono-dispersed particle size.

2.2.1. Van der Waals interactions

The van der Waals interaction between two spheres of the same radius R can, in general, be expressed as:

$$V_{VDW-SS} = -\frac{A_{H-SS}}{3} \left[\frac{R^2}{z^2 - 4R^2} + \frac{R^2}{z^2} + \frac{1}{2} \ln \left(1 - \frac{4R^2}{z^2} \right) \right] \quad (8a)$$

When the center-to-center separation z is much larger than the radius, this simplifies to [13]:

$$V_{VDW-SS} = -A_{H-SS} \frac{16 R^6}{9 z^6} \quad (8b)$$

The Hamaker coefficient A_{H-SS} is based on the materials of the two spheres and the medium that separates them. The Monte Carlo simulation domain is normalized by R , so these two formulas simplify to:

$$V_{VDW-SS} = -\frac{A_{H-SS}}{3} \left[\frac{1}{s^2 - 4} + \frac{1}{s^2} + \frac{1}{2} \ln \left(1 - \frac{4}{s^2} \right) \right], \quad \text{for } 2 < s < s_{\text{cutoff}} \quad (9a)$$

$$V_{VDW-SS} = -A_{H-SS} \frac{16}{9 s^6}, \quad \text{for } s > s_{\text{cutoff}} \quad (9b)$$

where $s = z/R$ is the nondimensionalized distance, which was varied to determine the minimum value s_{cutoff} for which accurate results are obtained. Eq. (9b) minimizes computation time by reducing operations in the energy calculations. As discussed in the results section, $s_{\text{cutoff}} = 50$ was selected to optimize the computational expense without sacrificing accuracy.

In addition to sphere–sphere interactions there are also sphere–plane interactions, where the plane represents the membrane. The van der Waals potential between a particle and a membrane surface is given by:

$$V_{VDW-SP} = -\frac{A_{H-SP}}{6} \left[\frac{R}{l} + \frac{R}{2R+l} + \ln \left(\frac{l}{2R+l} \right) \right], \quad (10a)$$

where l is the surface-to-surface distance between the particle and the membrane. This form holds for all separations, although

alternative forms which are computationally efficient exist for large separations and near-contact distances. Introducing the scaled coordinate $h = l/R$, this simplifies to:

$$V_{VDW-SP} = -\frac{A_{H-SP}}{6} \left[\frac{1}{h} + \frac{1}{2+h} + \ln \left(\frac{h}{2+h} \right) \right]. \quad (10b)$$

It has been noted that the van der Waals potential becomes infinite when particles approach the limit of contact. Thus a minimum separation distance between particles is imposed. If particles reach such a close proximity the move in the Monte Carlo step is rejected as if the particles had overlapped. A separation of roughly 0.158 nm has been suggested as the minimum distance between particles [14] and is used here.

2.2.2. Electrostatic forces

Electrostatic potentials are also present due to particle–particle and particle–membrane interactions. These potentials are governed by close-range and long-range interactions. The general close-range electrostatic force between two spheres is:

$$V_{EDL-SS} = \frac{64\pi a_1 a_2 \epsilon_0 \epsilon_r k_b^2 T^2}{(a_1 + a_2) z_e^2 e^2} \gamma_1 \gamma_2 \exp(-\kappa l), \quad (11)$$

where a_1 and a_2 are the radii, which here are both R , $l = z - 2R = R(s - 2)$ is the separation distance between the shear planes of two spheres, and z_e is the electrolyte valence. The reduced surface potential is $\gamma = \tanh(z_e e \zeta / k_b T)$ and the Debye screening length is $\kappa = \sqrt{2 \times 10^3 N_A e^2 z_e^2 C_{EL} / \epsilon_0 \epsilon_r k_b T}$. The zeta potential ζ is particle dependent, but since all particles are taken to be the same, $\gamma_1 = \gamma_2 = \gamma$ in the sphere–sphere case. Eq. (11) then simplifies to:

$$V_{EDL-SS} = \frac{32\pi R \epsilon_0 \epsilon_r k_b^2 T^2}{z_e^2 e^2} \gamma^2 \exp(-\kappa l). \quad (12)$$

For long-range interactions the radii of both spheres plus the surface-to-surface distance appears in the denominator, and the simplified equation for like-spheres becomes:

$$V_{EDL-SS} = \frac{64\pi R^2 \epsilon_0 \epsilon_r k_b^2 T^2}{(2R + l) z_e^2 e^2} \gamma^2 \exp(-\kappa l). \quad (13)$$

With sufficiently small l this reduces to Eq. (12). Therefore Eq. (13) is used for nearly all separations, except for those in very close proximity when $l < l_{cutoff}$. A variety of additional electrostatic potential functions for various limiting criteria are given in Elimelech et al. [15].

The sphere–plane interaction, where the plane represents the membrane, is based on Eqs. (11) and (13), taking the limits of both equations as one radius goes to infinity, where both yield the same formula:

$$V_{EDL-SP} = \frac{64\pi R \epsilon_0 \epsilon_r k_b^2 T^2}{z_e^2 e^2} \gamma_1 \gamma_2 \exp(-\kappa l). \quad (14)$$

In this case $\gamma_1 \neq \gamma_2$ as the membrane and particles may have different zeta potentials.

It should be noted that the regions of formal validity for Eqs. (12) and (13) are $l \ll a_i$, $\kappa a_i > 5$ and $\kappa(2R + l) \gg 1$, $\kappa a_i \geq 10$, respectively. These formal conditions are not met for the 3.13 nm particles of BSA used in Section 4.1 as $\kappa a_i \approx 0.324$. Past works [16,17] have demonstrated that these approximations with similar inputs are valid well beyond their formal limits, as is often true for equations approximating EDL interactions [18]. For the 5 μm prototypical particles used in Sections 4.2 and 4.3 $\kappa a_i \approx 517$, based on the electrical characteristics of BSA.

3. Flow field and particle movement

3.1. Downstream crossflow continuum velocity field

A parabolic velocity profile based on a constant shear rate is an accurate approximation if the particles are uniformly distributed [6]. However, as the particles become more concentrated close to the membranes the crossflow velocity diverges from this Newtonian profile.

Here the velocity field is influenced by the local particle concentration through an apparent viscosity. The velocity field is solved and updated after each MC step. The fully developed, one-dimensional velocity profile is governed by the nondimensional momentum equation:

$$0 = -\frac{dP}{dx} + \eta(C) \frac{d^2 v_x}{dz^2} + \frac{d\eta}{dC} \frac{dC}{dz} \frac{dv_x}{dz}, \quad (15)$$

as in Hale et al. [19], where η is the Generalized Newtonian viscosity and C is the particle concentration. Eq. (15) assumes the system is in a quasi-steady state (the derivative of v_x with respect to time is negligibly small between Monte Carlo steps) and the flow is fully developed (there is no change in v_x with respect to the crossflow direction x). Furthermore, it is assumed that there is no flow normal to the crossflow, consistent with a permeate velocity that is much smaller than the crossflow velocity.

The velocity is impacted by the local viscosity, expressed as an exponential function of the concentration in the cell, $\eta(C) = \eta_0 \exp(\alpha C)$. The parameters η_0 and α are solution dependent and were extrapolated from experiments to be $\eta_0 = 0.8887$ and $\alpha = 0.0097$ [19]. The velocity boundary conditions imposed at the membranes are no-slip in the crossflow direction and negligible permeate flow in the normal direction (equivalent to no-penetration from the continuum perspective). This neglects the small permeate velocity as it is several orders of magnitude less than the crossflow. However permeate velocity does impact the particle transport as described by the hydrodynamic force. The pressure gradient is a derived parameter based on the crossflow Reynolds number Re_{cf} given by:

$$Re_{cf} = -\frac{1}{12} \frac{dP}{dx} \frac{\rho H^3}{\mu^2}, \quad (16)$$

where H is the channel height and ρ and μ are the density and absolute (dynamic) viscosity of water, respectively. Throughout these calculations, the properties of pure water at 300 K and 1 atm were used for the continuum media, with $\rho = 996.63 \text{ kg/m}^3$ and $\mu = 8.887 \times 10^{-4} \text{ kg/m s}$.

The concentration was determined by dividing the cell vertically about the Chebyshev–Gauss–Lobatto collocation points [20] used in the velocity field solution. A fit of the concentration was created as discussed below, and the velocity was then solved using a spectral collocation method with Chebyshev polynomials, with a resolution of 50 collocation points in z . The Chebyshev polynomials are defined by the recursion relation [21]:

$$T_0(z) = 1, \quad T_1(z) = z, \quad T_{n+1}(z) = 2zT_n(z) - T_{n-1}(z). \quad (17a-c)$$

The governing equation requires the first two derivatives of the Chebyshev polynomials, which are defined through similar recursion relations. The first derivative is described by:

$$T'_0(z) = 0, \quad T'_1(z) = 1, \quad T'_2(z) = 4z \\ T'_{n+1} = 2zT'_n(z) + 2T_n(z) - T'_{n-1}(z) \quad (18a-c)$$

and the second derivative follows in a similar manner.

The first derivative of the viscosity with respect to concentration is also required, which is simply the derivative of the exponential function given by $d\eta/dC = \alpha \eta_0 \exp(\alpha C)$. The derivative of

concentration with respect to the channel position dC/dz strongly influences the velocity field and the shear rate, given in simple shear flow as $\dot{\gamma}(z) = dv_x/dz$. The shear rate drives the shear-induced diffusivity in Eq. (6), so it is critical that not only the concentration profile is smooth, but its first derivative is also smooth.

3.2. Fit of particle concentration across the channel

Four different concentration interpolation schemes were tested: Chebyshev polynomials, a 4th order polynomial fit, cubic splines [22] and a piecewise linear fit. Piecewise linear interpolation was rejected because it did not provide sufficient smoothing and gave drastically different results from the other interpolants. The three remaining schemes were tested at six values of Re_{cf} : 0.1, 1, 10, 100, 500 and 1000. The following were recorded: the maximum velocity, the number of steps, the order parameter defined in Kim and Liu [6] as:

$$\Psi_{NP} = \left(\frac{1}{NP} \sum_{i=1}^{NP} z^2 \right) - \left(\frac{1}{NP} \sum_{i=1}^{NP} z \right)^2, \quad (19)$$

and the CPU time required for the order parameter to converge. Ψ_{NP} provides a basic measure of the proximity of the particles to the membranes and the degree of symmetry of the system in the z direction. When the order parameter reaches a steady value it generally indicates that the system has stabilized at the final steady state. The convergence rate and steady state of the simulation were used to determine the best choice for the concentration interpolation scheme for both computational efficiency and accuracy.

Cubic splines were selected as the preferred interpolation method for viscosity as they required the fewest steps to reach convergence in all simulations, remained stable and required the least amount of computational time. While, on average, a cubic spline step may take longer to complete compared to the other fits, the advantage of convergence in fewer steps still reduced computational time. Furthermore, simulations utilizing cubic splines were found to oscillate the least about the steady state equilibrium point, making it easier to interpret an appropriate value for the order parameter and maximum channel velocity.

3.3. Force Bias Monte Carlo

The velocity field determines the bias P_x with which particles are allowed to move in the direction of the crossflow, described by:

$$P_x = \frac{v_x(z)}{\max(v_x(z))}. \quad (20)$$

This bias determines the possible envelope of moves for each particle in the MC step via:

$$\begin{aligned} \Delta x &= a_0(2 \times rand - 1 + P_x)D_c \\ \Delta y &= a_0(2 \times rand - 1)D_c \\ \Delta z &= a_0(2 \times rand - 1)D_c, \end{aligned} \quad (21a-c)$$

where a_0 is the maximum move size allowed in any coordinate direction, and $rand$ is a random number between 0.0 and 1.0 from the intrinsic random number generator in FORTRAN 90. Note that P_x allows for the case in which the maximum velocity is not at the center of the channel.

The maximum value of v_x was found using Newton's method on the velocity field after each Monte Carlo step. The initial guess for the location of the maximum velocity was the location from the previous step. In the interest of computational efficiency, the method was only allowed 10 steps to converge to a location where the derivative of the velocity profile was less than 0.01, or the second derivative was near zero, in this case less than 10^{-8} in magnitude. If Newton's method failed to converge, the location of the assumed maximum velocity defaulted to the center of the channel and the next Monte Carlo step was carried out.

The maximum move size a_0 was adjusted every ten Monte Carlo steps to maintain the ratio of accepted to attempted moves at approximately 0.5. Movement in all three directions was scaled by a displacement correction factor D_c defined as $D_c = 0.1 + P_x$. This has no bearing on the energy state of the particles, but simply allows for particles in the center of the channel to move more readily than particles near the membranes, aiding convergence. Depending on the random number generated and the bias associated with the z location, a particle displacement in the crossflow direction $\Delta x/a_0$ can fall anywhere within the envelope in Fig. 3.

The displacement was scaled by a_0 , which varies with the state of convergence of the MC simulation. Initially $a_0 = 2R(\pi/6\phi)^{1/3}$ for all simulations, a fairly large value equal to roughly 3.5 particle radii for a 10% volume fraction, and it decreased as the simulation progressed to a stable final state, to maintain approximately a 50% move acceptance ratio.

The FBMC uses the hydrodynamic force and the change in particle energy state to determine the probability that a move is accepted, so long as there is no particle overlap. The probability of accepting a move is described in [6] as:

$$P_z = \min[1, \exp(-\beta\Delta E - \beta\lambda\bar{\mathbf{F}}_h \cdot \Delta\bar{\mathbf{r}})], \quad (22)$$

where $\beta = 1/k_bT$ and λ is the force bias coefficient, typically 0.5 [23,24]. In previous work the change in energy was neglected because particles were treated as electrostatically non-interacting hard spheres to observe only the effects of Brownian and shear-induced diffusion. Here the change in the energy of each particle is calculated and influences the probability that a move is accepted.

The impact of the acceptance ratio was tested at $Re_{cf} = 10$ using values of 0.3 and 0.7 in addition to 0.5. All other simulation

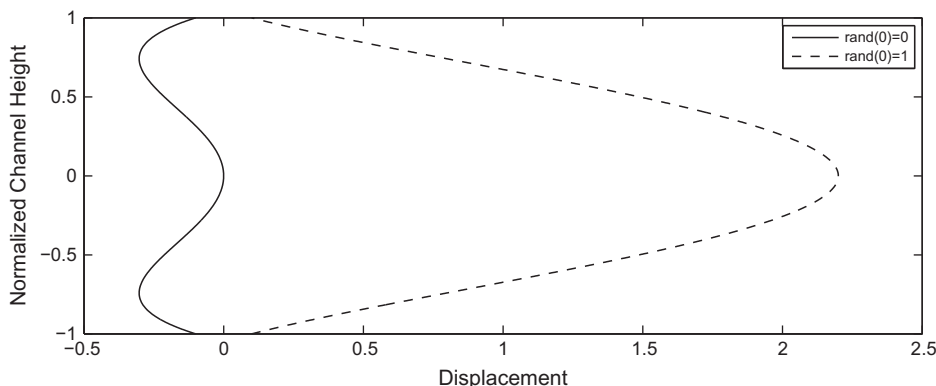


Fig. 3. Possible displacements scaled by a_0 based on a parabolic velocity field.

parameters were those given in Table 3. No significant change was observed in the steady state concentration field over this range of acceptance ratio.

4. Results and discussion for high (10%) particle fractions

First the impact of only electrostatic repulsion and van der Waals attraction is presented, with no flow and small 3.13 nm particles in Section 4.1. Then, only the impact of apparent viscosity is presented on the flow field in Section 4.2. In this case, electrical interactions are not considered and particles are increased to 5 μm . Finally, the combined effects are presented in Section 4.3 where the impact of the electrostatic double layer repulsion is shown to decrease the order parameter by forcing particles away from the membranes.

4.1. Migration of 3.13 nm particles due to electrostatic potentials and van der Waals interactions only

The sum of the potentials determines the energy state of each particle in a MC step. The energy states prior to movement and in the trial position are compared to find the change in energy. Here there is no fluid motion – the permeate flux is set to zero and there is no pressure differential and therefore no crossflow. The parameters used are for BSA (Bovine Serum Albumin), a common organic foulant used in experiments, and a prototypical membrane with the same parameters as BSA, given in Table 1 [16,17].

Five tests were carried out to see what cutoff value s_{cutoff} was sufficiently large for the separation of the particles to qualify as “much greater than” the radius of the spheres, for the purposes of computing the van der Waals potential using either Eq. (9a), (9b). The primary consideration was to find s_{cutoff} sufficiently large to achieve the correct final particle state. Convergence in s_{cutoff} was determined by the comparing steady state concentration fields for various cutoff values. A secondary consideration was computational run-time.

Values of $s_{\text{cutoff}} = 100, 50, 20, 5,$ and 3 were investigated. It was found that smaller cutoffs resulted in modest computational speed-up due to the reduction in the time to complete each MC step. However, the differences in the steady state concentrations fields for $s_{\text{cutoff}} = 3, 5$ and 20 were also significant, indicating that $s_{\text{cutoff}} = 3$ and $s_{\text{cutoff}} = 5$ were both too small to obtain accurate results. Increasing s_{cutoff} from 3 to 20 yielded increased order parameters associated with higher concentrations near the membrane.

Comparison of simulations with $s_{\text{cutoff}} = 50$ and 100 showed negligible differences in both run-time and the steady state solution. Therefore, the optimum cutoff falls in the range $20 < s_{\text{cutoff}} < 50$. Qualitatively speaking, the steady state solutions with

$s_{\text{cutoff}} = 20$ and 50 were sufficiently different to merit the larger cutoff. Furthermore, the increase in run-time from $s_{\text{cutoff}} = 20$ to $s_{\text{cutoff}} = 50$ was insignificant. Thus, $s_{\text{cutoff}} = 50$ was selected for all simulations to ensure independence of the solution on cutoff.

The cutoff value of the separation between shear planes of two particles l_{cutoff} at which the surface-to-surface separation of the particles is “much less than” the radius of the particles was also unknown. For l sufficiently small ($l < l_{\text{cutoff}}$) Eq. (12) can be used in place of Eq. (13) for the electrostatic double layer potential for sphere-to-sphere interactions. The value of l_{cutoff} was set at $0.1R$. Smaller values, for the case of BSA, would be near or below the minimum separation required for the van der Waals potential not to diverge. If the thickness of the Stern plane is neglected, l and s are related by $l \approx R(s - 2)$ and it is possible in some cases, though not mandatory, to relate l_{cutoff} to s_{cutoff} . However, because of the minimum separation s_{cutoff} for the van der Waals forces, this relationship was not enforced for the cutoff values and $l_{\text{cutoff}} = 0.1R$ throughout.

The electrostatic double layer repulsion dominates the van der Waals interactions. Since the membranes are assumed to carry the same charge as the particles, the repulsion from the membrane surfaces is the dominant effect. Even when coupled with the apparent viscosity impact on the crossflow, the electrostatic double layer still plays an important role in forcing particles away from the membranes, resulting in a reduced order parameter as shown in Section 4.3.

4.2. Flow modification influenced only by the apparent viscosity of 5 μm particles

As particles migrate toward the membrane surfaces during the Monte Carlo simulation, the viscosity in the core of the flow decreases, resulting in an increase in velocity in the core. An illustration of how the velocity develops as the Monte Carlo simulation progresses is shown in Fig. 4 for 10% particle volume fraction with parameters given in Table 2 and no electric interactions, demonstrating the dynamic nature of the profile.

For a fixed Re_{cf} the applied pressure gradient remains constant through all MC steps. However, the crossflow volumetric flow rate actually increases until the equilibrium condition is achieved. For all cases it was observed that the velocity fields at 5000 and 10,000 MC steps were almost identical, indicating the final state was reached. Initially, the particles are evenly distributed

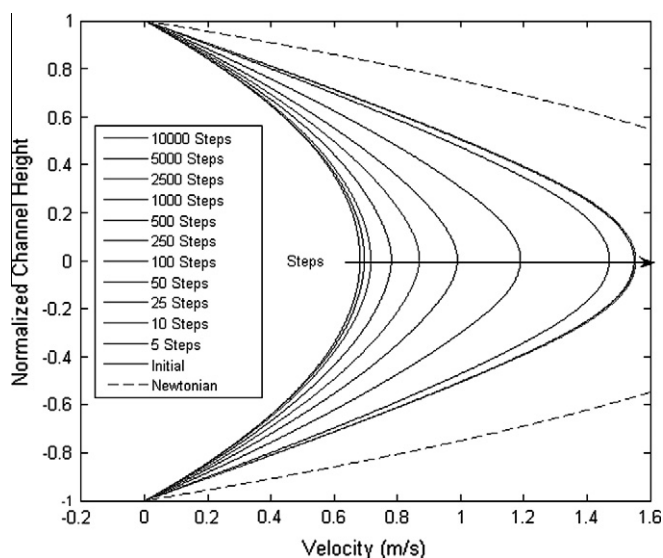


Fig. 4. Velocity profile development, $Re_{cf} = 1000$, for $\phi = 0.1$.

Table 1

Parameters used to study the impact of electric potential and van der Waals interactions with no continuum flow.

Particle volume fraction, ϕ	0.1
Number of particles	2100
Particle radius, R	3.13 nm
Cell size ratio ($W \times H \times L$)	$1 \times 7 \times 3$
Particle valence, z_p	-20
Permeate flux v_w	0 $\mu\text{m/s}$
Particle volume per mass [12]	0.729 mL/g
Electrolyte concentration, C_{EL} [17]	0.001 M
Particle-particle Hamaker constant, A_{H-SS} [12]	1.65×10^{-21} J
Temperature, T	300 K
Particle zeta potential, ζ [17]	-30 mV
Solvent dielectric constant, ϵ_r	78.54
Particle-membrane Hamaker constant, A_{H-SP} (estimate)	1.65×10^{-21} J
Electrolyte valence z_e [17]	1
Membrane zeta potential, ζ_{membrane}	-30 mV

Table 2

Parameters used to study the impact of apparent viscosity on the continuum flow, without electric or van der Waals interactions.

Particle volume fraction, ϕ	0.1
Number of particles	2100
Particle radius, R	5 μm
Cell size ratio ($W \times H \times L$)	$1 \times 7 \times 3$
Permeate flux v_w	30 $\mu\text{m/s}$
Particle volume per mass	0.729 mL/g
Temperature, T	300 K

Table 3

Parameters used when considering both apparent viscosity, electric and van der Waals interactions.

Particle volume fraction, ϕ	0.1
Number of particles	2100
Particle radius, R	5 μm
Permeate flux velocity, v_w	30 $\mu\text{m/s}$
Cell size ratio ($W \times H \times L$)	$1 \times 7 \times 3$
Particle volume per mass [12]	0.729 mL/g
Temperature, T	300 K
Maximum steps	10,000
Electrolyte concentration, C_{EL} [17]	0.001 M
Particle-particle Hamaker constant, $A_{H,SS}$ [12]	1.65×10^{-21} J
Particle zeta potential, ζ [17]	-30 mV
Solvent Dielectric Constant, ϵ_r	78.54
Particle-membrane Hamaker constant, $A_{H,SP}$ (estimate)	1.65×10^{-21} J
Membrane zeta potential, ζ_{membrane}	-30 mV
Electrolyte valence, z_e [17]	1

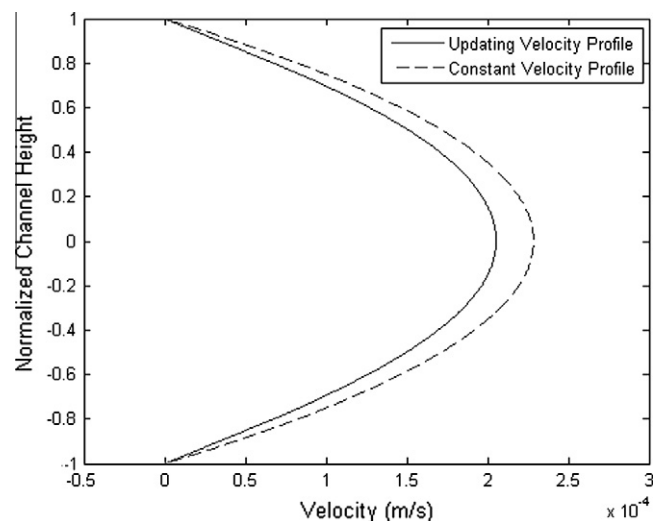
throughout the domain, resulting in a high apparent viscosity and a low flow rate. As most of the particles migrate toward the membranes and away from the center of the channel, the apparent viscosity in the interior drops. For a fixed pressure gradient, the velocity responds by increasing in the interior. This is consistent with a high initial concentration of contaminant, followed by recycling of the crossflow, which then becomes progressively cleaner.

For comparison, the Newtonian case without particles ($\alpha = 0$) is plotted to demonstrate the impact of the particles on the velocity field via the apparent viscosity. The Newtonian case with viscosity η_0 has the well known parabolic velocity profile of the form $u_x(z) = v_{\text{max}}(1 - z^2)$ where $v_{\text{max}} = Re_{cf} \times 2.285 \times 10^{-3}$ m/s for the parameters used. The steady state (final) velocity profile based on apparent viscosity (with particles) is only slightly modified for $Re_{cf} \leq 0.1$, as shown in Fig. 5. In contrast, at higher Re_{cf} there is significant flow modification as shown in Fig. 4. The differences in the velocity profiles are explained by the concentration profiles, discussed below.

Flow impediment compared to the Newtonian case is exaggerated by the high concentration of foulant present. While not realistic for industrial membrane filtration processes, this does allow for investigation of the extreme case of strong apparent viscosity impact on the crossflow.

To verify the validity of the apparent viscosity treatment in regions of high particulate concentration, a Darcy model was also tested on the $Re_{cf} = 1000$ case. In regions where the particle volume fraction exceeded 0.3 the local Re_{cf} was reduced by three orders of magnitude to match the Darcy assumptions. It was found that the maximum deviation between the velocity fields predicted by the Darcy model and by the apparent viscosity model was 2%. Thus, the apparent viscosity formulation is an accurate approximation for this flow field.

It should be noted that the similarity between the Darcy and apparent viscosity formulations is aided by the arrangement of this particular flow. Because the high particle concentrations occur near the membranes, the difference between the two solutions is small since the crossflow velocity is already significantly retarded

**Fig. 5.** Final velocity profile for $Re_{cf} = 0.1$, for $\phi = 0.1$.

by the no-slip condition. Future simulations will apply the apparent viscosity model only in regions of low concentration, and these will be matched to Darcy flow regions where the concentration is high. The velocity normal to the membrane will be treated in the same way, using a 2-D simulation with the cake regions treated as Darcy flow.

4.3. Fouling with combined apparent viscosity, electrostatic potentials and van der Waals interactions for 5 μm radius particles

Crossflow Reynolds numbers over the range $0.1 \leq Re_{cf} \leq 1000$ were studied. The parameters used were a combination of those from the previous two sections, as given in Table 3, with the larger 5 μm radius prototype particles. For brevity, the effects of electrostatic potentials and van der Waals interactions will collectively be referred to as electric interactions from this point forward. Findings indicate that the addition of the electric interactions (dominated by the electrostatic repulsion) to the hydrodynamic effects results in a much more stable final state. Variables representative of the state of the simulation, including the order parameter in Eq. (19), were recorded every 10 MC steps. In the cases discussed above where only the electric interactions or only the apparent viscosity effects were considered, the final state of the system was observed to oscillate about an approximately steady order parameter. When both effects are combined, the system reaches a final state that, for the first four decimal places in the order parameter, does not oscillate.

No particles are removed or added during the entire simulation, meaning the volume fraction remains constant throughout all MC steps. With $\phi = 0.10$, the initial maximum move size is approximately $a_0 = 3.47R$. As the particles approach a stable configuration the maximum displacement a_0 decreases due to the increased difficulty of locating a lower energy state.

While all simulations reach a steady state, the degree to which this state fluctuates differs between simulations. For comparison, without the electric interactions the maximum move size reached a steady state of approximately 0.006R for $Re_{cf} = 0.1$ and 1.6R for $Re_{cf} = 1000$. For the cases with both electric interactions (electrostatic and van der Waals) and apparent viscosity effects, the final steady state maximum step size decreases dramatically to approximately $4 \times 10^{-7}R$ for $Re_{cf} = 0.1$ and $7 \times 10^{-6}R$ for $Re_{cf} = 1000$, indicating that the particles have reached a very stable configuration. The speed at which the simulation converges also differs with and without electric interactions. With electric interactions it requires approximately 1160 and 1830 MC steps for the order

parameter to converge to 4 significant digits at $Re_{cf} = 0.1$ and 1000, respectively. Without electric interactions the simulation fails to stabilize beyond 2 significant digits in 10,000 MC steps at $Re_{cf} = 0.1$, and requires ~ 2150 steps at $Re_{cf} = 1000$ to stabilize to 3 significant digits.

The addition of the electric interactions generates a thin region near the membrane where the particles are, for the system studied, repulsed by the electric double layer. This is demonstrated by the final concentration profiles shown in Fig. 6. As Re_{cf} is increased from 10 to 100 and then 1000, more particles are remixed by the flow and remain in the interior of the channel. The maximum volume fraction at the membranes is reduced from approximately 0.5 for $Re_{cf} = 10$ to approximately 0.37 for $Re_{cf} = 100$ and 0.27 for $Re_{cf} = 1000$. Note that the regions near the core where the volume fraction dips below zero are not physical but are mild artifacts of the cubic spline fit.

At lower crossflow Reynolds numbers, the final profiles closely mimic a narrower channel with uniform Newtonian viscosity and a parabolic velocity field, similar to that observed for $Re_{cf} = 0.1$ without electric interactions in Fig. 5. The regions of high concentration (and therefore viscosity) near the membranes dissipate some of the energy, decreasing the maximum velocity that occurs in the center of the channel. In higher Reynolds number flows, the concentrations vary more gradually throughout the channel. This makes

the fluid appear overall more viscous with just a small internal core region of uniform viscosity, resulting in the sharp velocity profile observed in Fig. 6 for $Re_{cf} = 1000$. This larger region of higher viscosity dissipates much more energy, severely decreasing the maximum velocity in the channel as compared to the Newtonian case, equivalent to the reduction observed in Fig. 4 without electric interactions.

Without electric interactions the permeate flow draws the particles to the highest concentration against the membranes. The addition of electrostatic repulsion results in the particles being clustered near, but displaced off, the membrane. As the first term in the order parameter defined in Eq. (19) measures the proximity of the particles to the membranes, the order parameter is subsequently reduced at all Re_{cf} by this double layer effect which causes the highest concentration to occur slightly away from the membrane. The order parameter with and without the electric interactions is shown in Fig. 7.

The general trend of reduced order parameter with increasing Re_{cf} is preserved, but the electric double layer repulsion between the particles and the membranes shifts the order parameter down. In both cases the decrease in order parameter with increasing Re_{cf} is indicative of more particles remaining mixed into the flow in the core of the channel. A snapshot of a final (steady state) case with $Re_{cf} = 10$ is shown in Fig. 8, where the particle radius has been exaggerated for better visualization.

4.4. Comparison with related works

Cohen and Probstein [25] investigated colloidal fouling of reverse osmosis membranes and implied that fouling may be significant if permeate velocity is much higher than the threshold transmembrane velocity ($5 \mu\text{m/s} = 18 \text{lmh}$) and the colloidal solution is stabilized. In this work the permeate velocity was set to $30 \mu\text{m/s}$ and colloidal interactions were controlled using the Hamaker constant and zeta potential. Using a one-dimensional, transient, continuum model of colloidal deposition, Cohen and Probstein predicted a fast initial reaction-dominated fouling regime (formed within 0.02 s), followed by a very gradual convection-driven colloidal cake growth. To mimic these microscopic phenomena, a high particle volume fraction ($\phi = 0.1$) was used here to initiate the simulations. Monte Carlo simulations for investigating membrane deposition phenomena with realistic particle volume fractions of 0.0001–0.001 are practically impossible in terms of available computational resources. The initial random configuration of particles with $\phi = 0.1$ will reach a final configuration similar to that shown in Fig. 8. The concentration of particles near the channel epi-center then approximately mimics realistic feed volume fractions; and the deposition layers at the two membranes accurately predict the fouling layer formation. The MC simulations presented here are fundamentally different from solving deterministic, transient, continuum mass balance equations since the MC steps to reach a final dynamic equilibrium can flexibly follow various stochastic paths.

Early fundamental work of shear-induced transport was carried out by Davis and Leighton [26] and Leighton and Acrivos [10,11]. This work presented a relative viscosity, defined as the viscosity of a solution with particle volume fraction ϕ to that of a particle-free solution, represented by [11]:

$$\eta(\phi) = \left[1 + \frac{1.5\phi}{1 - \phi/\phi_c} \right] \quad (23)$$

where ϕ_c is the maximum packing density (0.58 for hard spheres). Later, this experimental correlation was widely used in various filtration theories. Note that the relative viscosity correlation is obtained in the absence of the permeate flux (perpendicular to the

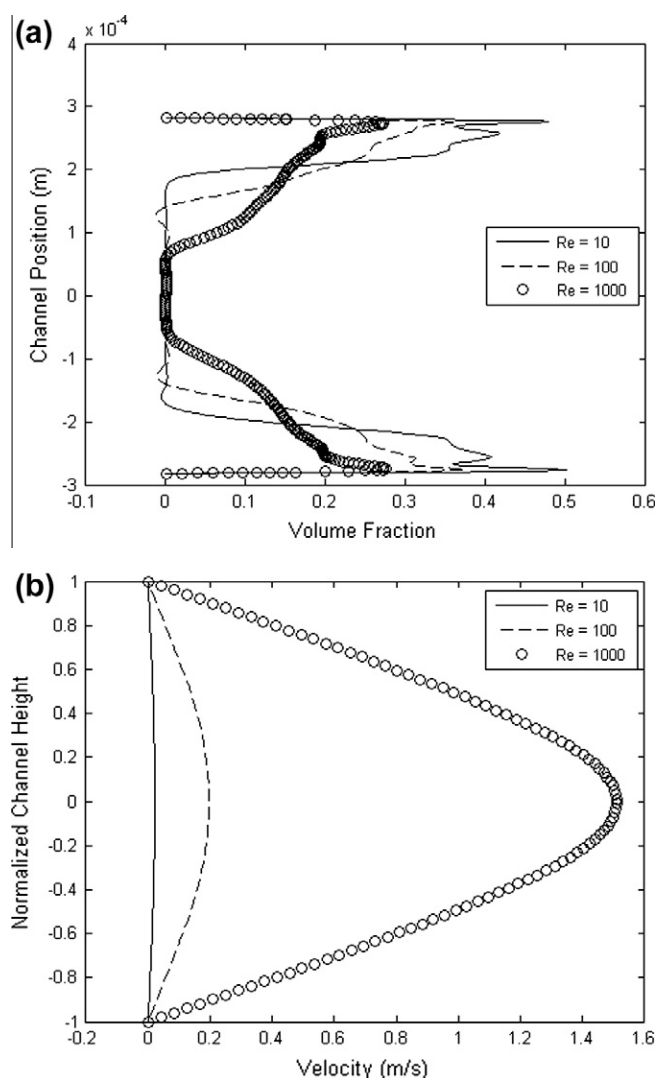


Fig. 6. (a) Final concentration profiles and (b) velocity fields for $Re_{cf} = 10, 100$ and 1000 with electric and van der Waals interactions for $\phi = 0.1$.

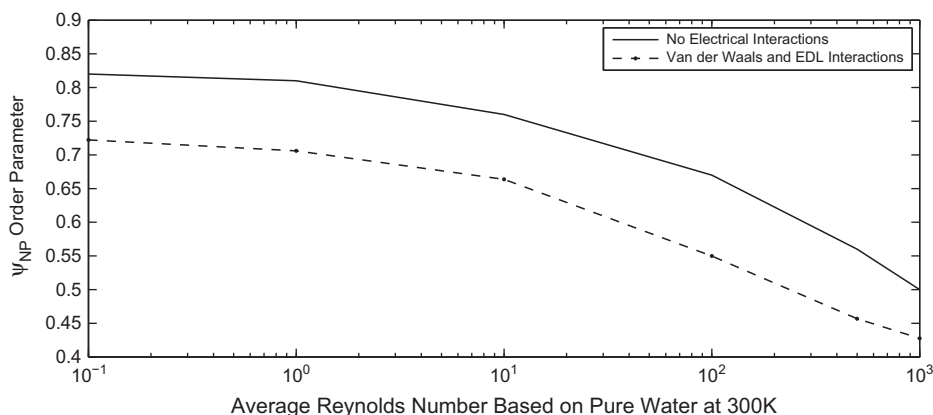


Fig. 7. Final order parameter comparison with and without electric and van der Waals interactions, over a range of Re_{cf} .

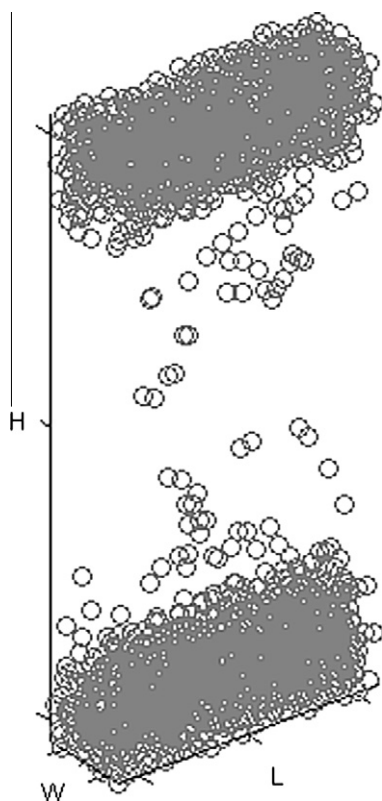


Fig. 8. Final state for $Re_{cf} = 10$ with electric and van der Waals interactions, for $\phi = 0.1$.

membrane surface), assuming particles are mono-dispersed hard spheres.

Sethi and Wiesner [27] incorporated the work of Davis and Leighton [26] in a unified model to include three particle transport mechanisms (Brownian diffusion, shear-induced diffusion, and inertial lift) and indicated that minimum fluxes occur in a particle size range of 0.01–0.1 μm , depending on operating time. Their unified model has two noticeable aspects related to diffusion and convection: (1) constant Brownian and concentration-dependent, shear-induced diffusion coefficients are superposed into an effective, combined form, and (2) the channel cross-section perpendicular to the crossflow direction is effectively reduced as the thickness of the solid cake layer grows. The effect of cake resistance is included in Darcy's law using the Carman–Kozeny correlation [28], but the sedimentation coefficient was not included in the

governing convection–diffusion equation for the particle transport. Instead, concentration-dependent viscosity was used to calculate the permeate flux as mutually influenced by particle volume fraction near the membrane surfaces. Note that their specific models for cake filtration, cake growth, and particle flux are at the continuum level of colloidal solutions.

In past work [9] an effective thermo/hydrodynamic force acted on a particle in a sheared flow of local volume fraction ϕ at temperature T , undergoing transverse permeate flux v_z , as expressed in Eq. (1). In this work, the continuum level calculation is related to the semi-microscopic MC simulation regime where the effective force exerted on each particle is calculated locally using configurations of adjacent particles. More rigorous forces can also be calculated using microhydrodynamics such as Stokesian dynamics and dissipative hydrodynamics [29].

In the semi-microscopic MC simulations presented here, the local viscosity is determined in a quasi-steady state of stable particle distributions after the system reaches a new thermodynamic equilibrium. A general investigation of the mutual influences of particle interactions and local shear rate is a very sophisticated and challenging task, and is out of the scope of the present research. But, particle–particle and particle-membrane interactions are implicitly included in calculations of apparent viscosity at pre-determined crossflow Reynolds numbers. The effective hydrodynamic force and particle interactions, described in Sections 2.1 and 2.2, respectively, allow for investigation of the apparent viscosity of the colloidal suspension near the membrane surface in various physical and chemical liquid states. Extension to bi- and poly-dispersed colloidal solutions and investigation of particle distribution (based on size) and (possible) stratification are potentially difficult in continuum theories due to lack of rheological information, but feasible tasks in future MC simulation research.

5. Conclusions and future studies

This work demonstrates the coupling of a Force Bias Monte Carlo method with a continuum flow solver via a generalized Newtonian viscosity function which depends on local particle concentration. In densely packed regions the apparent viscosity closely mimics a Darcy approximation, without the need to track or locate the boundary between the Darcy and inertial regions of the flow field.

The deposition of particles on the membrane or the mixing of particles into the free stream is strongly influenced by hydrodynamic forces. Higher shear rates associated with higher Reynolds numbers helped keep some particles mixed into the free stream. At lower Reynolds numbers all particles were attracted to the membrane forming a cake layer.

To consider what is collectively referred to here as electric effects, the energy of each particle was calculated based on van der Waals and electrostatic potentials. Each particle–particle potential is governed by two possible equations based on the separation. The close-range interaction form is generally more complicated and computationally intensive than the longer-range form. The appropriate cutoffs for both van der Waals and electrostatic potentials were determined by a series of tests to ensure converged results and maximum computational efficiency. It was found that combined electric and hydrodynamic effects result in a more stable final state as compared to the case with just hydrodynamic influence.

To demonstrate the coupling of the MC and continuum simulations a fully-developed velocity profile was assumed and an extreme case of 10% particle volume fraction was used. Future simulations will investigate more realistic fouling with 1% or lower volume fraction and 2-D flow fields, and include multiple particle types and membrane surface roughness. These simulations will help interpret the fouling observed in laboratory experiments with laminar crossflow such as those of Contreras et al. [2], Wang and Tarabara [4], and Chellam and Wiesner [30]. Particle trajectories predicted by FBMC will be compared to the trajectory theory developed by Chellam and Wiesner [31] for particles in laminar crossflow with clean membranes.

References

- [1] World Health Organization, Water, sanitation and hygiene links to health (2004).
- [2] (a) A. Contreras, A. Kim, Q. Li, J. Membrane Sci. 327 (2009) 1–2;
(b) A.S. Kim, A.E. Contreras, Q. Li, R. Yuan, Langmuir 25 (2009) 7815–7827.
- [3] R.S. Faibish, M. Elimelech, Y. Cohen, J. Colloid Interface Sci. 204 (1) (1998).
- [4] F. Wang, V.V. Tarabara, J. Colloid Interface Sci. 328 (2) (2008).
- [5] J. Happel, AIChE J. (1958) 4.
- [6] A.S. Kim, Y. Liu, J. Membrane Sci. (2008) 323.
- [7] D. Leighton, A. Acrivos, Chem. Eng. Sci. 41 (6) (1986).
- [8] A.S. Berman, J. Appl. Phys. 24 (9) (1953).
- [9] A.S. Kim, Y. Liu, Ind. Eng. Chem. Res. (2008) 47.
- [10] D. Leighton, A. Acrivos, J. Fluid Mech. (1987) 177.
- [11] D. Leighton, A. Acrivos, J. Fluid Mech. (1987) 181.
- [12] H. Chen, Y.S. Kim, J. Lee, S.J. Yoon, D.S. Lim, H.-J. Choi, K. Koh, Sensors 7 (10) (2007).
- [13] V.A. Parsegian, Van der Waals Forces: A Handbook for Biologists, Chemists, Engineers, and Physicists, Cambridge University Press, 2006.
- [14] R.J. Hunter, Foundations of Colloid Science, vol. 1, Oxford University Press, 1986.
- [15] M. Elimelech, J. Gregory, X. Jia, R.A. Williams, Particle deposition & aggregation: measurement, modeling and simulation. In: R.A. Williams, (Ed.), Colloid and Surface Engineering: Applications in the Process Industries; Controlled Particle, Droplet and Bubble Formation, 1995, Butterworth-Heinemann.
- [16] S. Bhattacharjee, A.S. Kim, M. Elimelech, J. Colloid Interface Sci. (1999) 212.
- [17] A.S. Kim, E.M.V. Hoek, Env. Eng. Sci. 19 (6) (2002).
- [18] W.C. Chew, P.N. Sen, J. Chem. Phys. 77 (4) (1982).
- [19] J.S. Hale, A. Harris, Q. Li, B.C. Houchens, ASME Int. Mech. Eng. Cong. Expo. (2007).
- [20] J.P. Boyd, Chebyshev and Fourier Spectral Methods, Dover Publications, 2001.
- [21] J.C. Mason, D.C. Handscomb, Chebyshev Polynomials, Chapman & Hall/CRC, 2003.
- [22] M.T. Heath, Scientific Computing: An Introductory Survey, McGraw-Hill, 2002.
- [23] M.P. D'evelyn, S.A. Rice, Chem. Phys. Lett. 77 (3) (1981).
- [24] M. Rao, B.J. Berne, J. Chem. Phys. (1979) 71.
- [25] R.D. Cohen, R.F. Probst, J. Colloid Interface Sci. 114 (1986) 194.
- [26] R.H. Davis, D.T. Leighton, Chem. Eng. Sci. 42 (1987) 275–281.
- [27] S. Sethi, M.R. Wiesner, J. Membrane Sci. 136 (1997) 191.
- [28] P.C. Carman, Trans. Inst. Chem. Eng. 16 (1938) 168–188.
- [29] A.S. Kim, Chem. Lett. 41 (2012) 1128–1130.
- [30] S. Chellam, M.R. Wiesner, Environ. Sci. Technol. (1997) 31.
- [31] S. Chellam, M.R. Wiesner, Environ. Sci. Technol. (1992) 26.